Bulletin of the Seismological Society of America, Vol. 80, No. 5, pp. 1079–1098, October 1990

RUPTURE PROCESS OF THE 1987 SUPERSTITION HILLS EARTHQUAKE FROM THE INVERSION OF STRONG-MOTION DATA

BY DAVID J. WALD, DONALD V. HELMBERGER, AND STEPHEN H. HARTZELL

ABSTRACT

A pair of significant earthquakes occurred on conjugate faults in the western Imperial Valley involving the through-going Superstition Hills fault and the Elmore Ranch cross fault. The first event was located on the Elmore Ranch fault, M_s = 6.2, and the larger event on the Superstition Hills fault, M_s = 6.6. The latter event is seen as a doublet teleseismically with the amplitudes in the ratio of 1:2 and delayed by about 8 sec. This 8-sec delay is also seen in about a dozen strong-motion records. These strong-motion records are used in a constrained least-squares inversion scheme to determine the distribution of slip on a 2-D fault. Upon closer examination, the first of the doublets was found to be itself complex requiring two episodes of slip. Thus, the rupture model was allowed to have three separate subevents, treated as separate ruptures, with independent locations and start times. The best fits were obtained when all three events initiated at the northwestern end of the fault near the intersection of the cross-fault. Their respective delays are 2.1 and 8.6 sec relative to the first subevent, and their moments are 0.4, 0.9, and 3.5 × 10^{25} dyne-cm, which is about half of that seen teleseismically. This slip distribution suggests multi-rupturing of a single asperity with stress drops of 60, 200, and 15 bars, respectively. The first two subevents were confined to a small area around the epicenter while the third propagated 18 km southwestward, compatible with the teleseismic and afterslip observations.

INTRODUCTION

The Superstition Hills earthquake sequence of 24 November 1987 occurred on the west side of the Imperial Valley of southern California (see Fig. 1). These events took place on a fault system consisting of the northwest-trending Superstition Hills fault and the conjugate, northeast-trending Elmore Ranch fault. The first main shock, the Elmore Ranch earthquake (M_s 6.2, 0154 GMT) along with its aftershocks and a wide distribution of predominantly left-lateral surface faulting, defines a northeast trend that was associated with left-lateral faulting at depth. Twelve hours later a second main shock, the Superstition Hills earthquake (M_s 6.6, 1315 GMT), initiated at the intersection of the northeast and southwest trends and was accompanied by right-lateral surface rupture of the Superstition Hills fault. This larger event is at least a doublet as observed teleseismically, and it is the rupture properties of this event that we address in this study.

Permanent strong-motion accelerographs in the epicentral region (Fig. 1) augmented by the timely placement of two portable stations by Doug Given of the USGS provide a valuable data set for investigating the rupture process. The complexity of the Superstition Hills earthquake rupture is revealed in the strong-motion records (see Fig. 2). In general, the acceleration recordings exhibit unusually long durations and relatively large amplitudes compared to other events of this magnitude. Three distinct subevents are recognized on most of the station recordings as indicated by arrows. In this study, we seek to explain the complexity of these strong-motion observations by determining the fault rupture history and slip distribution. We employ the finite fault waveform inversion procedure of Hartzell

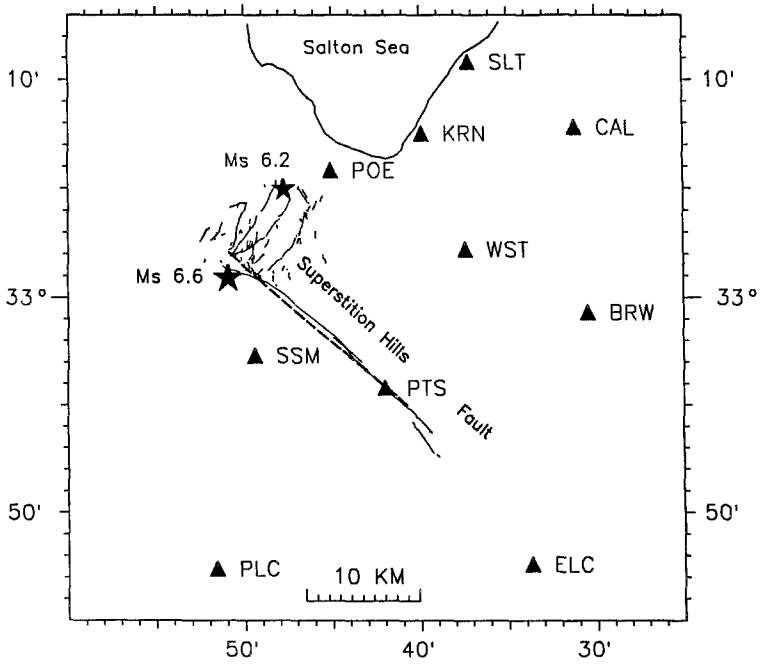

FIG. 1. Location map showing strong ground motion stations. Light lines show the extent of surface slip for both the Elmore Ranch and Superstition Hills earthquakes (epicenters are shown by asterisk). Temporary stations POE and KRN were put in place after the Elmore Ranch earthquake. The dashed line represents the fault segment used in the strong-motion inversion.

and Heaton (1983). This analysis allows us to describe both the temporal and spatial distribution of slip on the fault and attribute peak ground motion arrivals to specific regions of concentrated dislocation.

In an earlier study of the strong-motion records, Frankel and Wennerberg (1989) presented a rupture model for this earthquake derived from a tomographic source inversion of the strong-motion velocity recordings. An advantage of their tomographic inversion is that it requires no *a priori* assumption about each subevent location, rupture time, and rupture velocity. Their results present estimates of the timing, location, spatial extent, and rupture velocity for the three principal subevents for this earthquake, thus providing a useful starting point for this study. In their methodology, however, in order to invert the velocity seismograms for the slip acceleration as a function of time and yet limit the number of unknowns, a 1-D fault model was used. Further, Green's functions were represented by a delta function with amplitudes approximated by the effects of propagation, radiation pattern, and geometric spreading. In the present study, we represent faulting on a 2-D planar surface and employ Green's functions complete up to the frequency of 3 Hz, which includes the frequency band usually found adequately stable for this type of inversion (Hartzell and Heaton, 1983). Although the linear inversion employed in this study does require an *a priori* estimate of the average rupture velocity, source nucleation point, and subevent delay time, these values can be varied in subsequent runs over a reasonable range to recover the model parameters that are most consistent with the observations. This aspect of the inversion procedure will be discussed further.

An important question we address is the inconsistency between local and teleseismic models of this earthquake. Results of Frankel and Wennerberg (1989) suggest that high-frequency radiation is limited in spatial extent to the northern section of the Superstition Hills fault. This region is northwest of the fault stepover seen in Figure 1, 5 km northwest of station PTS. However, teleseismic studies that address the spatial distribution of the longer-period energy release (Bent *et al.*, 1989; Hwang *et al.*, 1990) require greater than 10 to 15 km of separation between the earlier subevents (subevents 1 and 2 as observed on the strong ground motions) and the later subevent (subevent 3 at local stations). These long-period and short-period results are mutually exclusive because subevent 3 of Frankel and Wennerberg (1989) is temporally correlated with the later teleseismic arrivals. That is, for the local and teleseismic models to both be correct, there would have to be rupture occurring simultaneously at two separate portions of the fault, one generating only short-period energy (northern portion of the fault) and the other only long-period energy (southern section of the fault). We attempt to resolve this issue.

The methodology we employ has previously been shown to provide valuable insight into the rupture history of other California earthquakes (Heaton, 1982; Hartzell and Heaton, 1983; Hartzell and Heaton, 1986; Mendoza and Hartzell, 1988a) as have other finite fault approaches (Olson and Apsel, 1982; Archuleta, 1984). In addition to providing information on the details of each rupture, these studies provide information about the characteristics common to these events. Mendoza and Hartzell (1988b) summarized these slip distribution models to note that large gaps in aftershock patterns often signify the regions that provide most of the energy release. From the distribution of slip, we can also place constraints on the location and depth extent of significant energy release and characterize the local stress drop of individual subevents. In this investigation, we add to the collection of earthquakes that were sufficiently well recorded to retrieve this type of source information. Our results provide an estimate of the spatial and temporal distribution of slip that will enhance such studies as cross fault interaction (Hudnut *et al.*, 1989) and fault segmentation (Rymer, 1989) of the Superstition Hills earthquake sequence.

Data and Initial Analysis

The locations of the strong-motion stations used in this study are displayed in Figure 1 as discussed earlier. The strong-motion station abbreviations used in Figure 1, the station locations, and the components used in the inversion are given in Table 1. Also depicted in Figure 1 is the extent of surface faulting associated

TABLE 1

Strong-Motion Stations

Abbreviation	Station	Latitude	Longitude	Components
POE	Poe Road	33.097	115.751	270,360
SLT	Salton Sea Wildlife Refuge	33.18	115.62	315
SSM	Superstition Mtn.	32.955	115.823	45,135
WST	Westmorland Fire Station	33.037	115.623	90,180
ELC	El Centro Imperial Valley County Center	32.793	115.562	0,90
PTS	Parachute Test site	32.93	115.70	225
KRN	Kornbloom Road	33.125	115.665	270,360
BRW	Brawley	32.988	115.50	315
CAL	Calipatria Fire Station	33.13	115.52	315
PLC	Plaster City	32.79	115.86	

with these two events (Sharp *et al.*, 1989). Accelerograms were hand digitized from copies of the USGS records (Porcella *et al.*, 1987) and were provided in digitized form by the CDMG (Huang *et al.*, 1987) for stations Westmorland (WST) and El Centro (ELC). We concentrate primarily on the horizontal strong-motion records of the Superstition Hills earthquake for the following reasons. The strong velocity increase with depth in the Imperial Valley results in arrivals predominantly at near vertical incidence, thus isolating P waves on the vertical and S waves on the horizontal components. Consequently, the vertical components of motion are, in general, higher in frequency and smaller in amplitude and therefore more difficult to accurately hand digitize as well as model (given our limited knowledge of the local velocity structure and constraints on computer time). Further, because of the difficulty in modeling high frequencies, velocity records rather than acceleration records are used in the inversion. The velocity records, obtained by integrating the acceleration recordings, are shown in a profile in Figure 2. For display purposes, the records in Figure 2 have been aligned in time on the peak motion of subevent 2, the easiest arrival to recognize at all stations, and have been rotated to the back azimuth of the epicenter to obtain "tangential" components. While this rotation is

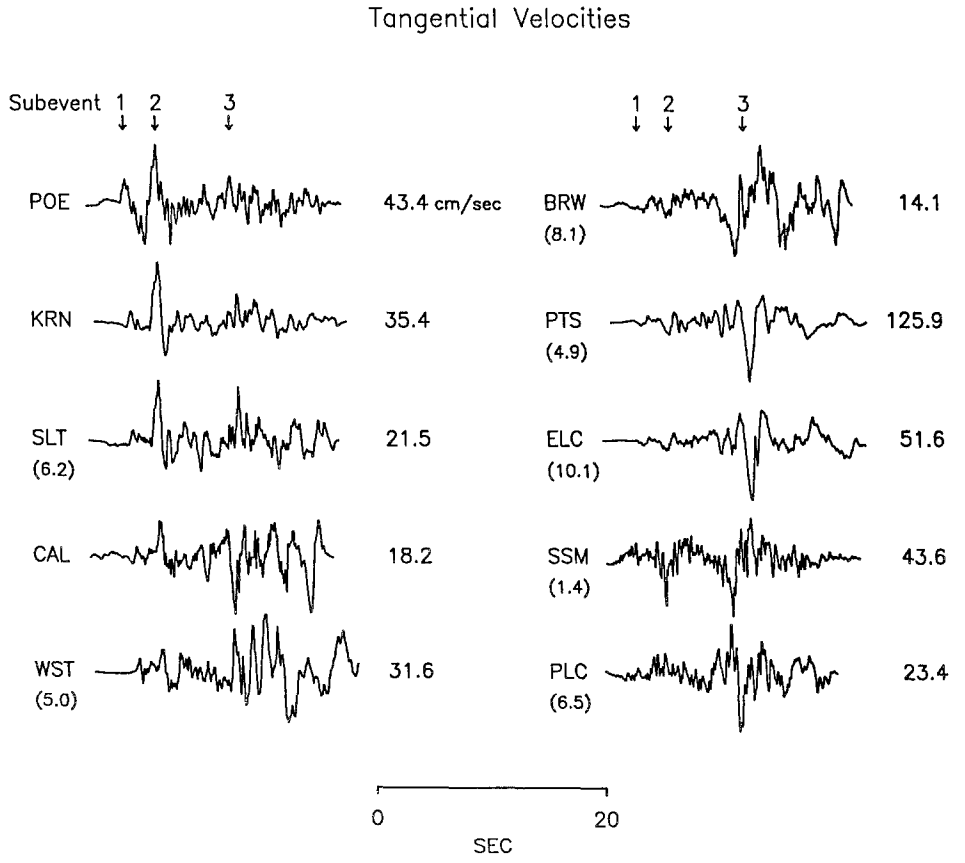

FIG. 2. Tangential velocity recordings of the Superstition Hills earthquake obtained by rotating horizontal components to the back azimuth of the epicenter. Arrows indicate the approximate times of the three subevents. All traces are normalized to their peak value and are aligned vertically by the peak arrival of subevent 2. The time in seconds of the beginning of each trace after the origin time (1315:56.5 GMT) is given in parentheses below each record for which absolute time is available.

correct for the energy originating near the epicenter, it is only approximate for source regions further southeast along the fault.

Three subevents can be traced from station to station. A very good detailed analysis of these subevents has been provided by Frankel and Wennerberg (1989), and here we review some of the features they discuss and bring out additional observations critical to our study. It can be seen that the time separation between the first two subevents shows little variation. The consistency of the 2-sec time separation at stations covering a wide range of azimuths requires a common source region with a limited extent and separate ruptures for these two subevents. The third subevent shows more variation with azimuth, suggesting a more extended rupture zone. As this subevent is delayed at least 6 sec from the second and yet begins rupturing near the other subevents (Frankel and Wennerberg, 1989), it too requires a separate rupture initiation.

A most interesting feature of the observed velocity recordings is the apparent variation of directivity effects from subevent 2 and 3, most pronounced at stations directly towards the northeast (POE, KRN, and SLT) and southeast (PTS and ELC). This observation is examined in the tangential records shown in Figure 3. On the left hand side of this figure, the records are normalized to their peak values, while the waveforms on the right are all scaled to the peak amplitude of station

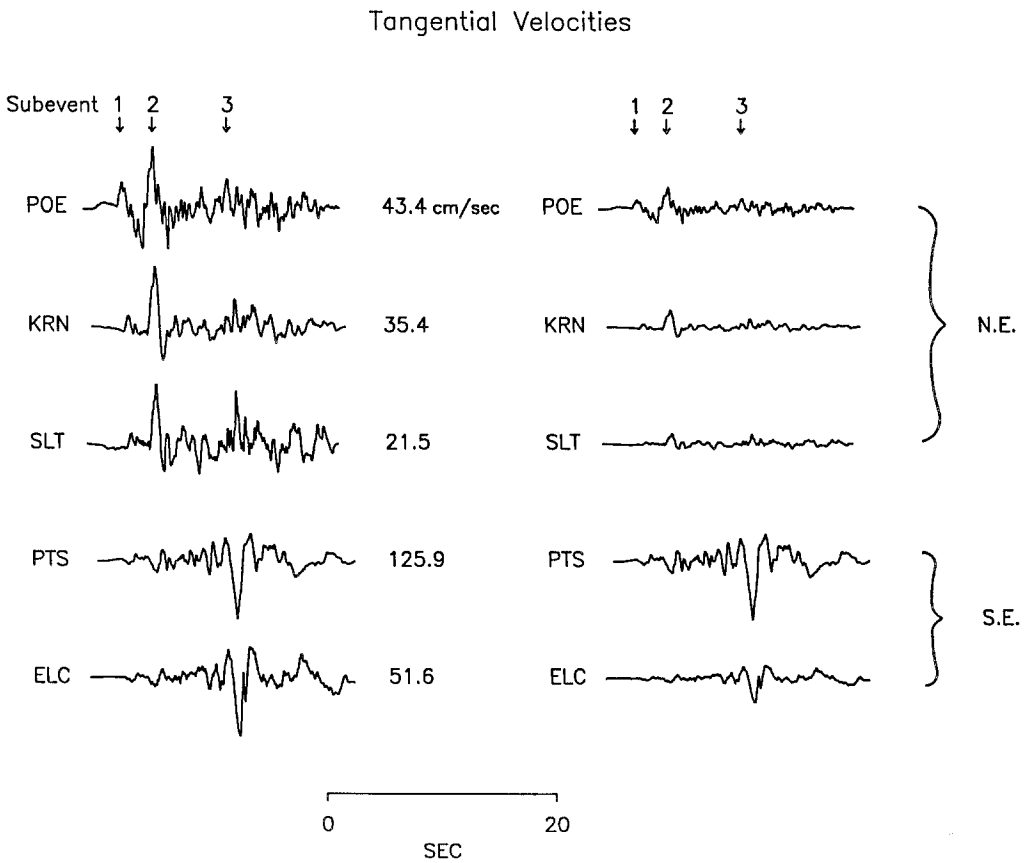

FIG. 3. Comparison of tangential velocity recording from stations at northeast (POE, KRN, SLT) and southeast (PTS, ELC) azimuths. The records on the left hand side are normalized to their peak values. The waveforms on the right are scaled to the peak amplitude of station PTS.

PTS. With the exception of those stations directly towards the northeast, subevent 3 produces the dominant arrival at each station and provides the peak velocity amplitude. This is consistent with teleseismic modeling results (Bent *et al.*, 1989; Hwang *et al.*, 1990) which show that, on average, the seismic moment computed for the third subevent is roughly twice that of the combined first and second subevents. In sharp contrast, the northeastward stations are dominated by arrivals produced by subevent 2 and show less prominent arrivals due to the third subevent. However, from the right side of the figure, it can be seen that the absolute amplitude of the second subevent is comparable in both directions if one compares stations at similar distances, that is PTS is between POE and KRN in terms of distance from subevent 2. These observations can be explained by a spatially compact subevent 2 which produces no significant directivity and a large southeastward rupture for the third subevent producing strong directivity effects in that direction. This is further substantiated by the uniformity of the pulse width of subevent two at all stations, which is approximately 2 sec, and the variation of the total duration of subevent 3, which is from 3 sec at PTS to over 8 sec at stations towards the northeast.

The location of the initial rupture plays an important role in the inversion scheme. This poses a difficulty in that there is a discrepancy between the reported hypocentral depth (2 km) determined from the regional network data (Magistrale *et al.*, 1989) and the greater depths determined for the first subevents from waveform modeling (9 km from Frankel and Wennerberg, 1989; 10 km, Bent *et al.*, 1989; 5 km, Hwang *et al.*, 1990). Careful inspection of the strong-motion accelerograms for the closest stations shows a clear shear-wave arrival approximately 1.0 to 1.5 sec before the onset of subevent 1. This suggests that the shallow 2 km network hypocentral depth may represent an earlier small preshock, as suggested by Bent *et al.* (1989). The simplicity of the shear-wave arrivals for the first two subevents allowed Frankel and Wennerberg (1989) to estimate their common location near the epicenter, but closer to the intersection of the two fault zones (Fig. 1). Although the depth determination for these subevents is not well constrained, synthetic seismograms computed for depths shallower than about 6 km show much more complexity than the subevent 1 and 2 observed waveforms. Furthermore, Bent *et al.* (1989) found that a shallow rupture was inconsistent with the surface waves observed at the Pasadena station (PAS, about 250 km northwest of the epicenter). We therefore adopt the depth of 9 km as chosen by Frankel and Wennerberg (1989) for our rupture initiation, although we later test deviations from this value. The initiation of subevent 3 is not impulsive at most stations and therefore could not be located from arrival times alone. The nucleation point of the third subevent was assumed to be at the same location of subevent 1 and 2, again based on Frankel and Wennerberg (1989), and it too was allowed to vary in subsequent forward models.

Fault Rupture Model and Inversion Method

The fault parameterization and modeling procedure we employ is that of Hartzell and Heaton (1983) in their study of the 1979 Imperial Valley earthquake. Faulting is represented as slip on a planar surface which is discretized into a number of subfaults. The total ground motion computed at a given station can be represented as a linear sum of the contributions of all the subfault elements, each appropriately delayed in time to simulate propagation of the rupture front. Formal inversion procedures are then used to deduce the slip distribution of these subfaults that minimizes the difference between the observed and synthetic strong motions.

In this study, we represent the Superstition Hills earthquake rupture with a vertical fault plane, striking 127°. Previous studies of the teleseismic recordings (Bent *et al.*, 1990; Hwang *et al.*, 1990; Sipkin, 1989; Dziewonski *et al.*, 1989) indicate some uncertainty in the dip value but on average suggest a near vertical fault. These studies indicate little scatter in the fault strike. We also assume that only right-lateral strike slip motion is significant. The small vertical component of slip and the numerous reversals of northeastward and southwestward scarp directions observed along the surface trace (Sharp *et al.*, 1989) suggest predominantly right-lateral motion on a vertical fault plane. We therefore assume that a vertical fault is the best fault plane representation of the majority of the moment release. We chose a fault length of 20 km and depth extent of 12 km based on the distribution of aftershocks (Magistrale *et al.*, 1989) with an additional constraint on the length by the extent of surface faulting (see Fig. 1). This area is then discretized into 20 subfault elements along strike and 10 elements downdip, giving each subfault a length of 1 km and a vertical width of 1.15 km.

The ground motion contribution for each subfault is computed using the Green's function summation and interpolation method of Heaton (1982) and Hartzell and Helmberger (1982). The subfault synthetics are obtained by summing the responses of a number of point sources over its area, each delayed in time in order to account for the propagation of the rupture front across the subfault. Thus, each subfault ground motion properly includes the effects of directivity. The point source responses or Green's functions, are computed for a gradient velocity model with the discrete wavenumber/finite element (DWFE) methodology of Olson *et al.* (1984) for frequencies up to 3.5 Hz. In practice, we calculate a master set of synthetics for increments of depths from 0.5 to 12 km and for ranges between 0 and 50 km, to allow for the closest and furthest possible subfault-station combinations. Then, for each subfault-station pair, the required subfault response is derived by the summation of 25 point source responses obtained by the linear interpolation of the closest Green's functions available in the master set. The linear interpolation of adjacent Green's functions is performed by aligning the waveforms according to their shear-wave travel times.

The subfault synthetics are convolved with a dislocation time history which we represent by the integral of a triangle with a total duration of 0.5 sec and equal rise and fall times. This time function was chosen based on a comparison of the synthetic velocity pulse width for a single subfault with the shortest duration velocity pulse width observed as well as on prior experience with this inversion method. Initially, we tried longer slip durations (0.7 and 0.8 sec), but found them to be inadequate.

The velocity model, shown in Figure 4, was chosen from the refraction study of Fuis *et al.* (1982) (their Fig. 22, approximately 20 km southeast of shotpoint 13) to represent an average velocity for the station paths in this study. This model is clearly an approximation of the true structure. Fuis *et al.* (1982) show significant lateral velocity variations in this region, especially in the vicinity of the Superstition Hills fault where buried basement scarps and changes of the thickness of sediment cover are evident. The variations in local depth to bedrock in relation to rupture on the Superstition Hills fault is discussed by Magistrale *et al.* (1989), Hwang *et al.* (1990), and Frankel and Wennerberg (1989).

Although lateral velocity variations will not be incorporated in the present study, as an effort to minimize their effects, we introduce static delay times in the waveform inversion procedure to account for travel-time differences. These corrections and the effects of complex local velocity structure will be discussed in the following section.

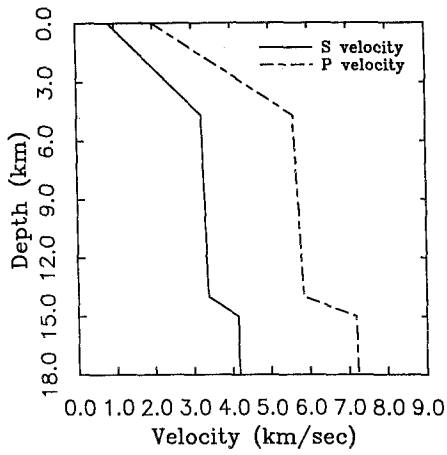

FIG. 4. Velocity structure used to compute strong motion synthetics. This model was derived from Fuis *et al.* (1982). See text for details.

The rupture velocity is assumed to be a constant 2.4 km/sec, or 75 per cent of the shear-wave velocity in the majority of the source region (Fig. 4). This parameter was varied to test its sensitivity in different inversion runs. Some flexibility in the rupture velocity is obtained by introducing time windows (Hartzell and Heaton, 1983). In their representation, each subfault slips when the rupture front reaches it and again in two successive time windows, effectively allowing for the possibility of afterslip or a locally slower velocity. In our formulation, we allow each subevent the flexibility of both a locally slower and faster rupture velocity by allowing slip during the time windows preceding and following that of the equivalent constant velocity rupture front. Each time window is separated by 0.5 sec.

A constrained, damped, least-squares inversion procedure is used to obtain the subfault dislocation values that give the best fit to the strong-motion observations. The inversion is stabilized by requiring that the slip is everywhere positive and that the difference in dislocation between adjacent subfaults (during each time window) as well as the total moment is minimized. These constraints have been previously addressed by Hartzell and Heaton (1983).

Both the observations and subfault synthetics are bandpass-filtered from 0.1 to 3.0 Hz with a zero phase Butterworth filter and are resampled at a rate of 20 samples per second. The upper frequency limit is imposed by the frequency range for which Green's functions can be conveniently calculated. Resampling reduces the number of points required in the point-by-point inversion scheme. Initially the synthetic and observed waveforms are aligned in absolute time when possible (trigger times were not available for stations CAL, KRN, and POE) and are then later adjusted for variations in travel time by aligning the initial shear-wave arrival from subevent 1 with the synthetic shear-wave energy from the subfault containing the initiation of rupture (hypocenter). While this provides an approximate static station delay, it will not improve timing errors introduced by lateral variations encounted by subfault to station travel paths that vary significantly along the fault.

Station PLC is not included because it is located in a region with a velocity profile significantly different than the average Imperial Valley velocity model used here. Moreover, ray paths from the northeast portion of the fault to PLC

transverse a different velocity structure than from the southeast section. A similar argument may be made for station SSM, which sits atop a bedrock nob, but since this site is so close to the fault, energy arriving at this station travels a near vertical path and can therefore be more easily adjusted with a static correction. All station observations are scaled to a unit amplitude in the inversion in order to insure equal importance of smaller amplitude stations and to downweight possible side effects. Although each station can be individually weighted to adjust for noisier records, all components were weighted equally.

Inversion Results

The distribution of strike slip dislocation for each subevent resulting from our preferred rupture model (No. 307) of the Superstition Hills earthquake is shown in Figure 5. Slip contours are in intervals of 40 cm with the maximum value for each subevent indicated in the figure. The large contour interval is used to emphasize robust features in the model and minimize the importance of smaller details. These dislocations represent the combined slip for the three time windows previously mentioned. This series of subevents can be regarded as a magnitude 5.6 earthquake followed 2.1 sec later by a larger, higher stress drop event of magnitude 6.0. Finally, after 8.6 sec, the same region ruptured a third time resulting in a magnitude 6.4 event that continued to rupture over a length of 18 km with considerable slip on the southern section of the Superstition Hills fault. A comparison of the observed velocity records and the synthetic waveforms produced by this model are shown in Figure 6.

An attempt was made to determine the most favorable location for the nucleation point of subevent 3. From the small, concentrated rupture area of subevent 2, it seemed reasonable that further slip during the subsequent subevent 3 might have initiated at the southeast edge of the zone that ruptured during subevent 2. However, this assumption gave results inferior to the model in which subevent 3 initiated at the location of the previous subevents. The rupture velocity of our preferred model is 2.4 km/sec. We also modeled faster rupture velocities for both subevent 2 and 3 to evaluate the waveform fits and the resulting slip distribution. Allowing a rupture velocity of 4 km/sec for subevent 2, approaching the 5.3 km/sec value suggested by Frankel and Wennerberg (1989), does not improve our model. Similarly, a rupture velocity of 2.7 km/sec (85 per cent of the local shear velocity) for the third subevent increases the misfit between the observations and the synthetics.

In an effort to resolve an interesting question of whether the first two subevents may have ruptured northeastward (Wald and Somerville, 1988; Frankel and Wennerberg, 1989) we ran an inversion in which rupture begins 2 km from the northwest end of the inferred Superstition Hills fault plane (Fig. 1) and propagates towards the northeast for both subevent 1 and 2. The resulting slip model produces synthetics with slightly better waveform fits to stations POE, KRN, and SLT, but which overpredict the observed subevent 2 amplitudes at these stations. The improvement in waveform fit is partially due to slip occurring on subfaults nearer to those stations, allowing more free model parameters with which to fit the observations. However, this model substantially underpredicts the subevent 2 amplitude at SSM, a result also seen in Frankel and Wennerberg's (1989) model for northeast rupture. The absence of aftershocks from the Superstition Hills earthquake along the northeast trend tends to further downplay the possibility of slip on the scale required by subevent 2 (Frankel and Wennerberg, 1989).

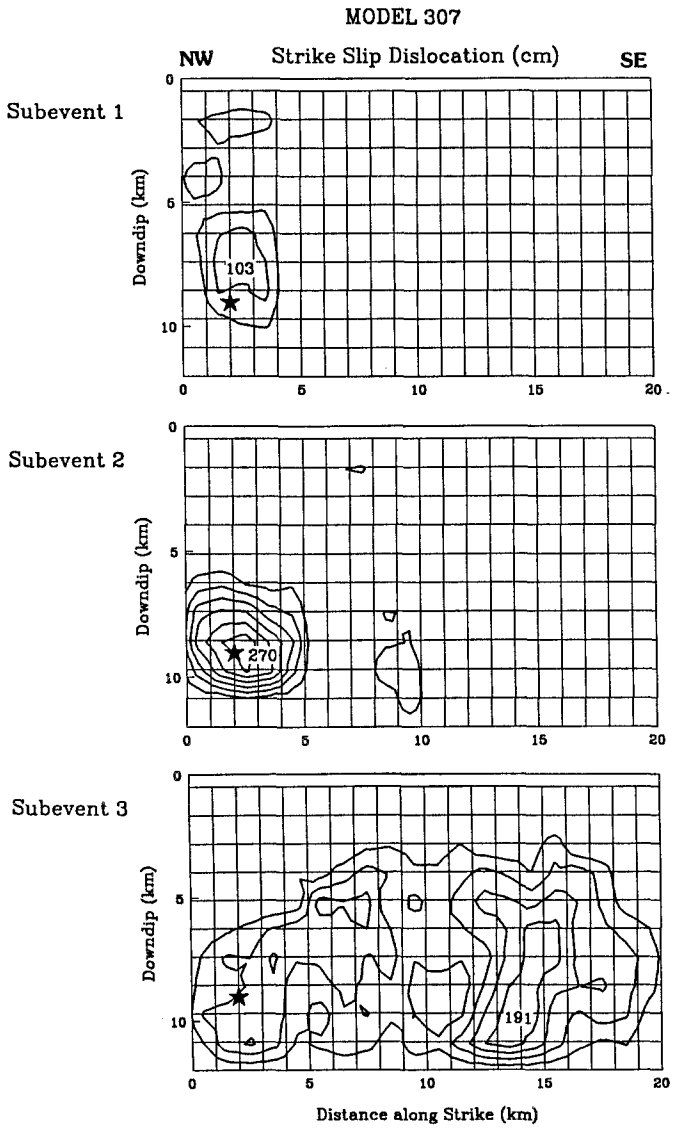

FIG. 5. Northwest–southeast cross section of the fault model showing subfault layout. Contours of strike-slip dislocation in centimeters for model 307 are given for each subevent. The contour interval is 40 cm. The peak slip value for each subevent is indicated.

Although three separate time windows were allowed for each subevent, slip occurred only during the first 0.5-sec window for the first two subevents, implying that the rupture timing of these smaller subevents was adequately modeled with a constant rupture velocity and that the true source-time function can be adequately simulated with a simple triangle. For the third subevent, significant slip occurred in the first two time windows and minor dislocation during the third window, although almost all subfaults individually had slip in only one of the available time windows (Fig. 7). This observation suggests that although the slip function for the third subevent can be modeled with a relatively simple time function, the rupture velocity was variable. Rupture on the northern section of the Superstition Hills fault required a velocity slightly faster than the constant value of 2.4 km/sec chosen

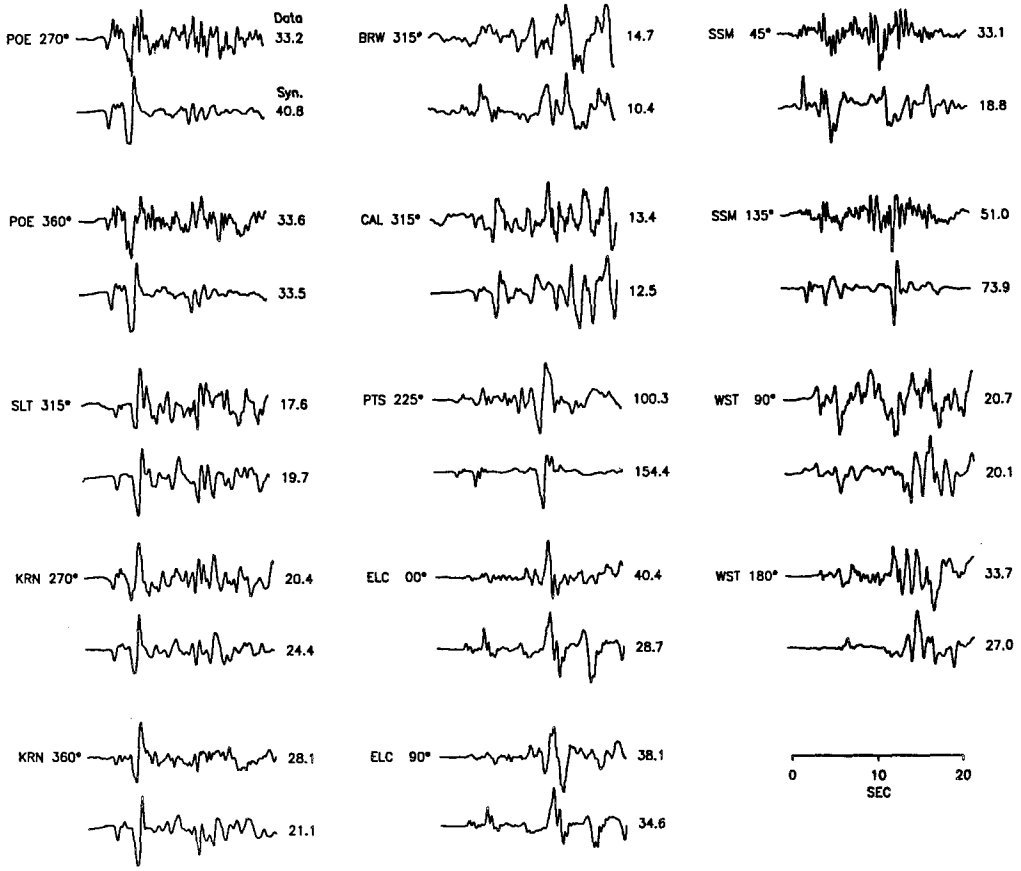

FIG. 6. Comparison of the observed (top trace) and synthetic (bottom trace) strong-motion velocity records for dislocation model 307 (shown in Fig. 5).

for the model (Fig. 7, time window 1), while rupture on the southern section of the fault required a rupture velocity close to the constant value (Fig. 7, time window 2). The spatial variation in the rupture velocity appears to coincide with a right step-over observed at the surface of the Superstition Hills fault (Fig. 1). This step-over also delimits a change from northwest to southeast in the physical behavior of the fault. At this location there is a change in the depth to basement rock along the fault and a corresponding change in the behavior of the seismicity (Magistrale *et al.*, 1989).

An additional explanation for the necessity of the time windows for the last subevent may be that its extended rupture into the southern section of the Superstition Hills fault results in a more complex series of propagation paths to each station, creating timing errors in our 1-D Green's functions. This can be seen at ELC, where the synthetic phase *SS* arrives earlier than the corresponding observed phase, and at SSM where the third subevent arrival on the 45° component arrives slightly late. Processed aftershock data from well located events would greatly help resolve these discrepancies in timing. Perhaps then the effects of lateral velocity variations on the resulting slip distribution can be evaluated. Note that, due to the complexity of the Superstition Hills earthquake, there is always the possibility of a tradeoff between the subevent delay time and the location of the subevent nucleation and the rupture velocity. The multiple subevents of this earthquake, each being independent ruptures, make a unique solution difficult to obtain.

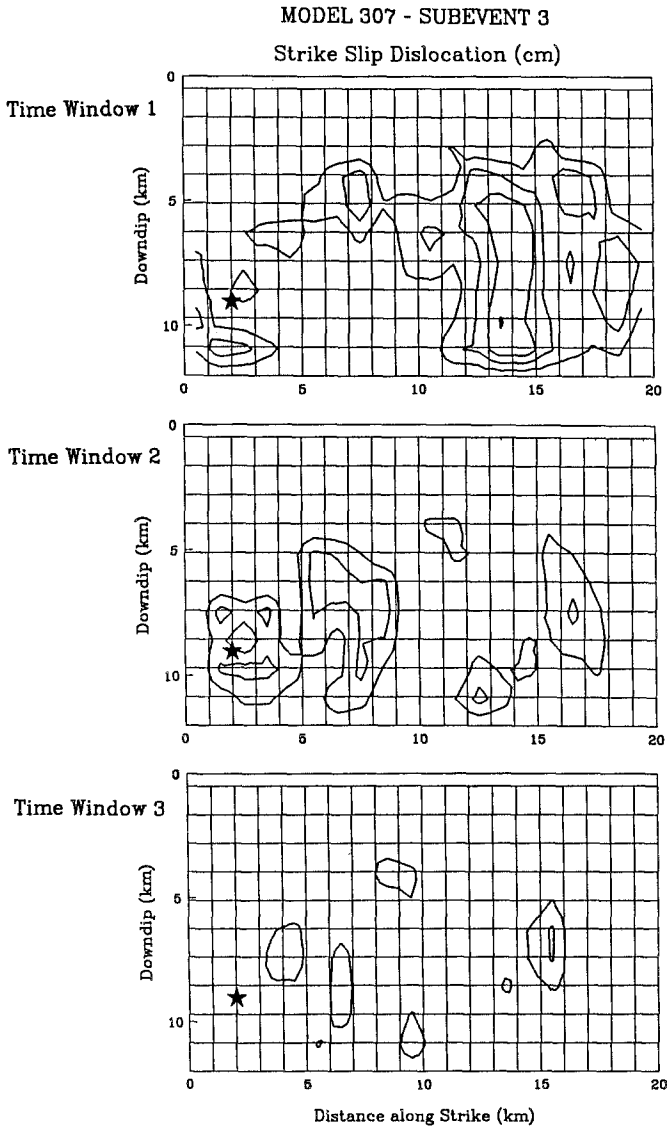

FIG. 7. Subevent 3 dislocations for time windows 1 (*top*), 2 (*middle*), and 3 (*bottom*). Each time window is separated by 0.5 sec. The contour interval is 40 cm.

The time delay of 2.1 sec between subevents 1 and 2 along with their depths are well constrained. Minor modifications of these parameters result in degradation of the fits to the waveforms. Variations in the delay time between subevents 2 and 3, however, strongly affect the results of the slip distribution for the third subevent (Fig. 8) without substantially degrading the waveform fits. A short delay (8.1 sec) for subevent 3 allows the rupture to propagate to the southern section of the fault (Fig. 8, *top*). As the delay time increases to 8.6 sec, moment release is forced deeper (Fig. 8, *middle*). Finally, if delayed by 9.1 sec (Fig. 8, *bottom*), slip is forced closer to the point of rupture nucleation along the deep, northwest portion of the fault. In order to resolve the extent of high-frequency radiation toward the southern portion of the Superstition Hills fault, we compare waveforms at selected stations (see Fig. 9) that are the most sensitive to the subevent 3 slip distribution. This

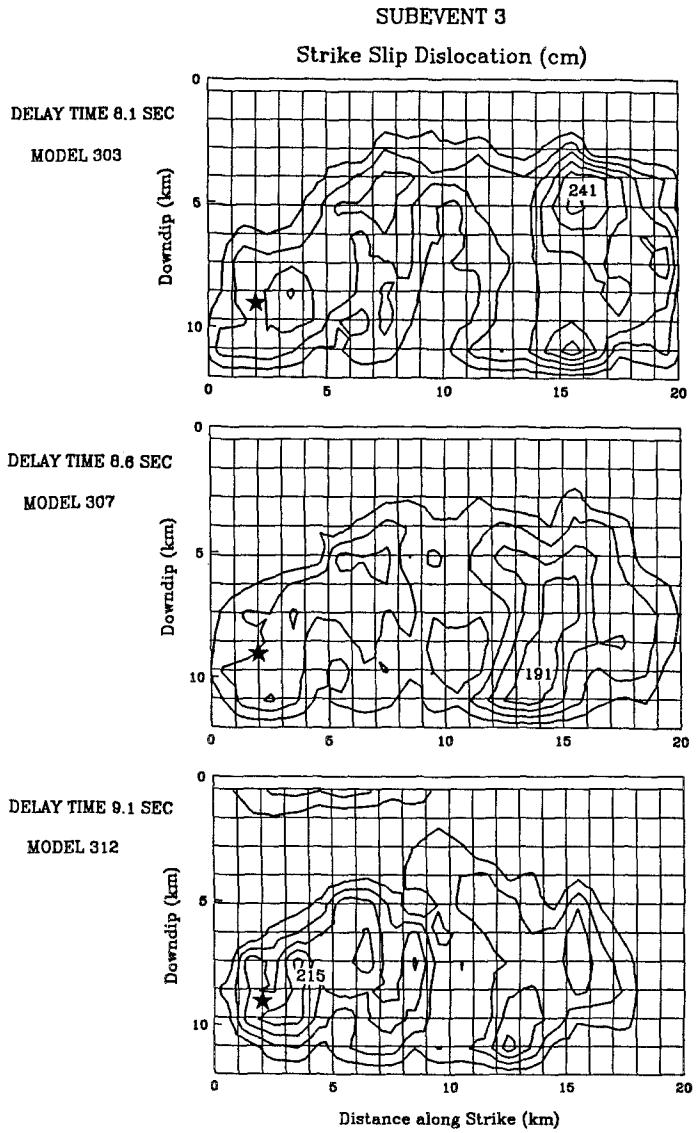

FIG. 8. Comparison of subevent 3 dislocation models for delay times of 8.1 sec (*top*, model 303), 8.6 sec (*middle*, model 307), and 9.1 sec (*bottom*, model 312). The peak slip values are indicated.

comparison is made for the inversion models shown in Figure 8. A summary of the inversion model parameters for different delay times is given in Table 2. The misfit between the data and the synthetics is given in terms of the Euclidean norm of the residual vector, $\| b - Ax \|$, and the variance, defined as the square of the Euclidean norm divided by the number of degrees of freedom. The number of degrees of freedom is equal to $N - 1$, N being the number of data points in the inversion minus the number of nonzero model parameters in the solution. It can be seen from Table 2 that in terms of the Euclidean norm and the variance, the difference in waveform fits is not dramatic. Further, the Euclidean norm can be misleading when comparing waveforms dominated by a few large amplitude arrivals. These factors suggest that other considerations be included in evaluating these models.

The shallow concentration of slip shown in model 303 (near 15 km) is not

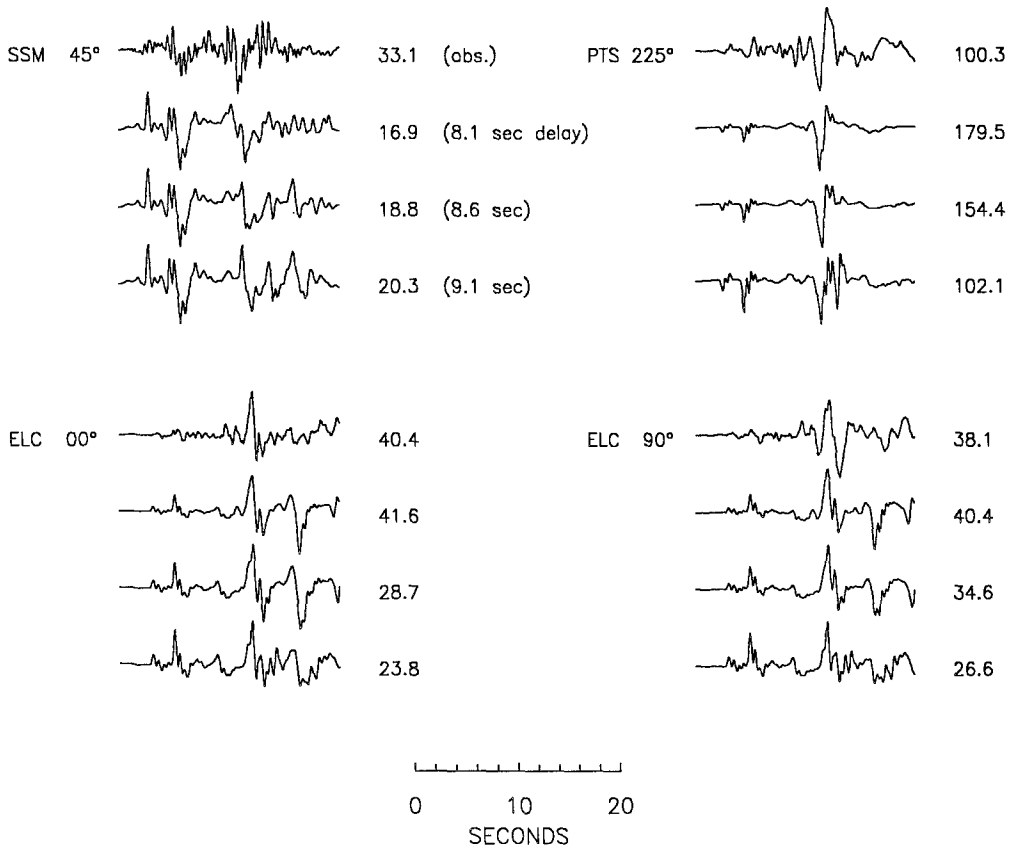

FIG. 9. Comparison of observed velocity records (top trace) with subevent 3 synthetics produced by the models shown in Figure 8 for selected stations. The synthetics shown are for delays of 8.1 sec (second trace), 8.6 sec (third trace), and 9.1 sec (bottom trace).

TABLE 2

INVERSION MODELS AND SUBEVENT PARAMETERS

Model	$\|b - Ax\|$	*Variance*	*Subevent*	*Time Lag* (*sec*)	*Moment* ($\times 10^{25}$)	Maximum Slip (cm)
303	18.52	0.0605	1	0.0	0.40	94
			2	2.1	0.84	253
			3	8.1	3.95	241
307	18.78	0.0636	1	0.0	0.44	103
			2	2.1	0.91	270
			3	8.6	3.46	191
312	19.10	0.0654	1	0.0	0.51	121
			2	2.1	1.06	326
			3	9.1	3.00	215

consistent with the lack of observed surface waves at the Pasadena station (Bent *et al.*, 1989, Fig. 2) or the moderate level of surface waves at ELC. This shallow slip also overpredicts the peak amplitude at PTS and produces a larger synthetic *SS* phase at ELC (Fig. 9, 2 sec from end of trace) than the observed phase. It should be noted that the *SS* phase at ELC in the synthetics is also earlier than the observed phase, indicating a laterally slowing velocity structure towards ELC may be more

appropriate than the 1-D model used here. A longer delay of 8.6 sec (model 307 in Fig. 8) for the start of subevent 3 yields a dislocation model more consistent with the surface-wave observations mentioned above and has the effect of moderating both the *SS* phase at ELC and the PTS amplitude. Model 312 with the longest delay time shown, 9.1 sec, has slip concentrated closer to the rupture nucleation and further reduces the *SS* arrivals at ELC, but it underpredicts the subevent 3 amplitudes at these stations. This results in subevent 3 to subevent 2 amplitude ratios inconsistent with the observations. It also degrades the waveform fit at PTS considerably. From these observations we favor the rupture model resulting from a delay time of 8.6 sec.

Discussion and Conclusions

A comparison of our preferred dislocation model (No. 307) with results of previous studies is presented in Figure 10 and summarized in Table 3. This figure is a northwest-southeast cross section along the Superstition Hills fault. Symbols in Figure 10 represent point sources, and line sources are denoted by bold face arrows. The strong-motion line source model favored by Frankel and Wennerberg (1989) is depicted as a solid circle leading into two overlapping arrows at a depth of 9 km. The solid circle represents their subevent 1; the circle up to the first arrow displays their subevent 2, starting about 2.5 sec later; and the circle up to the second arrow (to a distance of 10 km), starting 9.7 sec after the first subevent, represents their third subevent. The first two subevents in our model are nearly equivalent to those of Frankel and Wennerberg (1989), considering the comparison is between 1-D and 2-D fault models. There is, however, a substantial difference in the two strong-motion solutions for the third subevent. While subevent 3 in the Frankel and Wennerberg (1989) model begins about 9.7 sec after the first subevent and is limited in rupture length to about 8 km, our solution indicates a rupture length of over 18 km delayed by 8.6 sec. Our solution is not so different, however, from the slip distribution presented by Frankel and Wennerberg (1989) for a line source at a depth of 5 km (their Fig. 5). In fact, if one were to combine the slip acceleration of both the 5 and 9 km depth line sources depicted by Frankel and Wennerberg (1989) into a 2-D fault model, it is quite similar to the spatially extended subevent 3 we describe. Further note that our model 312, where we constrain the third subevent lag time to be 9.1 sec, is more limited in length. Model 312 is similar to the Frankel and Wennerberg (1989) model for a 9-km-deep line source but produces inferior waveform fits compared to model 307 and is further discounted for reasons that follow.

Of the teleseismic studies for this earthquake (Table 3), both Bent *et al.* (1989) and Hwang *et al.* (1990) attempt to resolve the spatial and temporal separation of moment release. The model of Bent *et al.*, (1989) is not represented in Figure 10 but includes two point sources separated in time by 7.5 sec. Their first subevent is located at a depth of 10 km, just below but within the location of our combined subevent 1 and 2. Their second subevent is greater than 6 km in depth and at a distance of more than 10 km from their first subevent. Similarly, Hwang *et al.* (1990) require significant source separations. They present two similar source models, a two point source model (large squares in Fig. 10) and a point source-line source combination (large square and dashed, bold arrow). In both teleseismic models, the first point source is consistent with the combined subevent 1 and 2 sources in our model and in the Frankel and Wennerberg (1989) model, although their 5 km source depth is shallower. However, their rms errors shows little change

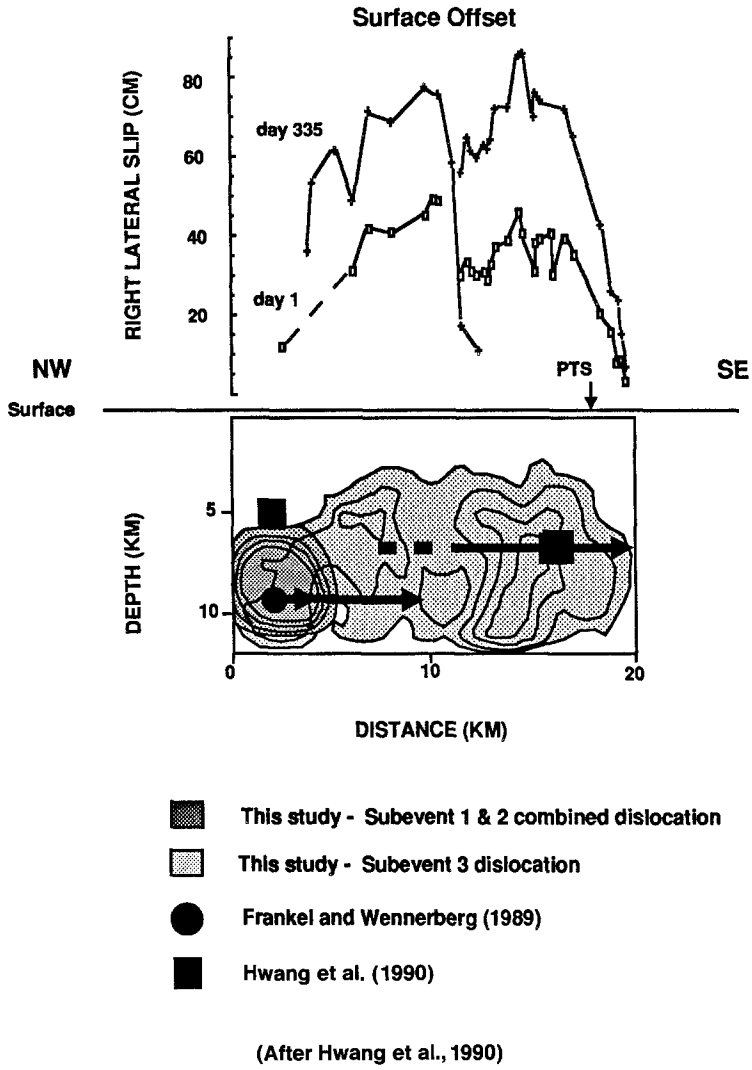

FIG. 10. Northwest–southeast cross section parallel to the Superstition Hills fault comparing dislocation model 303 with previous studies. The distribution of slip is shown with contours of 40, 80, 120, and 160 cm for subevent 1 and 2 combined (dark stipple) and subevent 3 (light stipple). The line source model of Frankel and Wennerberg (1989) is depicted by the circle and arrows (depth of 9 km). The solid squares and dotted line plus arrow represent the two models of Hwang *et al.* (1990). The top portion of the figure indicates afterslip 1 and 355 days after the earthquake (after Williams and Magistrale, 1989). See text for details.

with depths up to 5 km deeper than their chosen depth, indicating a greater source depth is also consistent with their data. As indicated in Figure 10, both the point source and line source teleseismic representations of the later moment release overlay the major region of slip in our third subevent, and the time separation is given as 8.1 sec by Hwang *et al.* (1990).

Both these teleseismic studies, as well as our model, suggest significant moment release on the southern section of the Superstition Hills fault. This is consistent with the distribution of the aftershocks, which extend beyond the mapped surface rupture. Furthermore, considerable afterslip at the surface occurred along the southern section (Williams and Magistrale, 1989) shown atop Figure 10, suggesting

TABLE 3

COMPARISON OF MODEL PARAMETERS

Model	Subevent	Moment ($\times 10^{25}$ dyne-cm)	Depth (km)	Time Separation (sec)
Model 307	1	0.44	6–9	0.0
	2	0.91	8–10	2.1
	3	3.46	6–10	8.6
Frankel and Wennerberg (1989)	2	0.47	9	2.5
	3	1.4	9	9.5
Hwang *et al.* (1990)	1 & 2	2.4	4	0.0
	3	5.2*	6	8.1†
Bent *et al.* (1989)	1 & 2	3.6	10	0.0
	3	7.2	>6	7.5†
Sipkin (1989)	total	10.2	10	
Dziewonski *et al.* (1989)	total	7.2	15	

* Hwang *et al.* (1990) model No. 1, two point sources.

† Time separation with respect to the first teleseismic subevent, which is made up of two subevents, 1 and 2, as seen on the strong ground motion recordings.

substantial slip at depth. The horizontal scale is common for both the top and bottom portions of this figure. Considerable afterslip occurred on both the northwest and southeast strands of the fault (Fig. 1), consistent with our model of dislocation at depth. The agreement between the longer-period teleseismic models, our strong-motion modeling results, and the afterslip at the surface favors moment release along the southern portion of the Superstition Hills fault radiating both short- (1 sec) and long-period (20 sec) energy.

The relative amount of moment release for individual subevents obtained from different studies is shown in Table 3. The teleseismically determined moment ratio of the second to first subsource is roughly 2 to 1, while the strong-motion studies have an average ratio (subevent 3 to subevent 1 and 2 combined) of 3 to 1. We expect that the strong motion studies, with a long-period cut off of 10 sec, might have smaller overall moment values than observed teleseismically (period of 15 to 20 sec). The total moment determined from model 307 is 4.8×10^{25} dyne-cm, or half the average teleseismic moment of 8.9×10^{25} dyne-cm. The total moment of the Frankel and Wennerberg (1989) strong-motion model is 1.87×10^{25} dyne-cm, one fifth the average teleseismic moment. Their low moment with respect to our model 307 may reflect the absence of moment release along the southern portion of the Superstition Hills fault in their model.

We may estimate the stress drop for individual subevents of the Superstition Hills earthquake, keeping in mind that these estimates are clearly dependent on the choice of rupture area. The region of nonzero slip varies with the amount of smoothing constraint chosen in the inversion. Therefore, in these calculations, we assign the area of rupture to be the region with slip greater than 20 per cent of the peak slip value for that subevent. The stress drop expression of Eshelby (1957) for a circular fault, $\Delta\sigma = (7\pi\mu\bar{u})/(16a)$, where μ is the rigidity, $\bar{u}$ is the average dislocation, and a is the radius, is suitable for subevents 1 and 2 considering their spatial distribution of slip (Fig. 5). For subevent 1, using $\mu = 3.3 \times 10^{11}$ dyne/cm^2, $\bar{u} = 40$ cm, and $a = 2.8$ km, we find a stress drop of 64 bars. Subevent 2, with $\bar{u} = 145$ cm and $a = 3.1$ km, has a stress drop of 207 bars. Subevent 3 has a stress drop of 87 bars using the same expression for a circular rupture and choosing a radius of 4.6 km and an average slip of 90 cm for the high slip area between

10 and 20 km (see Fig. 5, *bottom*). An alternative expression for stress drop for the entire subevent 3 rupture area is given by Knopoff (1958) for a long-shallow strike slip fault, $\Delta\sigma = (2\ \mu\bar{u})/(\pi w)$, where w is the fault width or depth. For $w = 9.5$ km and $\bar{u} = 70$ cm, the stress drop for subevent three over its entire rupture length is 15 bars.

Figure 11 shows the well located aftershocks ($M > 3.0$) of the Superstition Hills earthquake projected on the inferred fault plane together with the slip distribution of the major subevents as shown in Figure 10. The aftershocks tend to cluster along the shallow northern region and along a vertical section of the central portion of the fault. Aftershocks in the central portion of the fault separate regions of major slip on the northwestern and southwestern segments of the fault and underlie the fault stepover shown in Figure 1 and discussed earlier. The concentration of aftershocks outside regions of large slip has been observed for most earthquakes for which the coseismic slip has been determined from modeling. This observation has been interpreted by Mendoza and Hartzell (1988b) as resulting from the redistribution of stress following the primary failure on the fault plane. The relationship between aftershocks and regions of large slip during the Superstition Hills earthquake as seen in Figure 11 is clear, but is perhaps not as dramatic as seen in the examples presented by Mendoza and Hartzell (1988b).

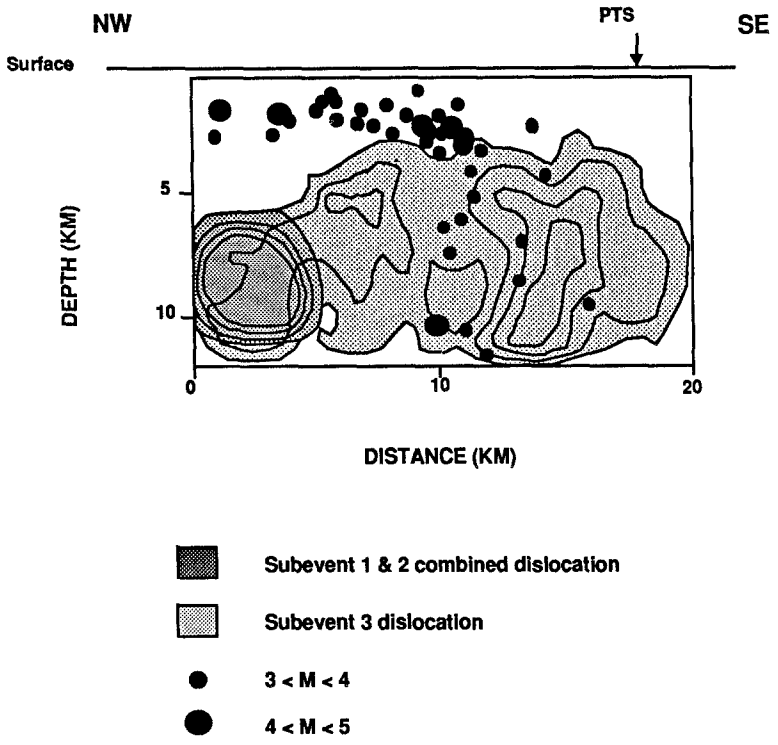

FIG. 11. Cross section of fault showing aftershocks ($M \geqq 3.0$) projected onto the fault plane. Also shown is the combined subevent 1 and 2 slip contours and the subevent 3 contours as shown in Figure 9. Contour interval is 40 cm.

ACKNOWLEDGMENTS

We thank Lorraine Hwang and Harold Magistrale for informative and useful discussions related to this paper. Reviews by Tom Heaton, Hiroo Kanamori, and Lisa Wald improved the original manuscript and critical reviews by Arthur Frankel and Paul Spudich helped clarify the presentation significantly. This work was supported by the USGS under contract 14-08-0001-21912. Contribution No. 4830, Division of Geological and Planetary Sciences, California Institute of Technology, Pasadena, California.

REFERENCES

Archuleta, R. (1984). A finite faulting model for the 1979 Imperial Valley, California, earthquake, *J. Geophys. Res.* **89,** 4559–4585.

Bent, A. L., D. V. Helmberger, R. J. Stead, and P. Ho-Liu (1989). Waveform modeling of the November 1987 Superstition Hills earthquake, *Bull. Seism. Soc. Am.* **79,** 500–514.

Dziewonski, A. M., G. Ekström, J. H. Woodhouse, and G. Zwart (1989). Centroid-moment tensor solutions for October–December 1987, *Phys. Earth Planet. Interiors* **54,** 10–21.

Eshelby, J. D. (1957). The determination of the elastic field of an ellipsoidal inclusion and related problems, *Proc. Roy. Soc. London, Series A* **241,** 376–396.

Frankel, A. and L. Wennerberg, (1989). Rupture process of the M_s 6.6 Superstition Hills earthquake determined from strong-motion recordings: application of tomographic source inversion, *Bull. Seism. Soc. Am.* **79,** 515–541.

Fuis, G. S., W. D. Mooney, J. H. Healy, G. A. McMechan, and W. J. Lutter (1982). Crustal structure of the Imperial Valley Region, in *The Imperial Valley, California, earthquake of October 15, 1979, U.S. Geol. Surv. Profess. Pap. 1254,* 25–50.

Hartzell, S. H. and T. H. Heaton (1983). Inversion of strong ground motion and teleseismic waveform data for the fault rupture history of the 1979 Imperial Valley, California earthquake, *Bull. Seism. Soc. Am.* **73,** 1553–1583.

Hartzell, S. H. and T. H. Heaton (1986). Rupture history of the 1984 Morgan Hill, California, earthquake from the inversion of strong motion records, *Bull. Seism. Soc. Am.* **76,** 649–674.

Hartzell, S. H. and D. V. Helmberger (1982). Strong-motion modeling of the Imperial Valley earthquake of 1979, *Bull. Seism. Soc. Am.* **72,** 571–596.

Heaton, T. H. (1982). The 1971 San Fernando earthquake: a double event?, *Bull. Seism. Soc. Am.* **72,** 2037–2062.

Huang, M. J., T. Q. Cao, C. E. Ventura, D. L. Parke, and A. F. Shakal (1987). CSMIP strong motion records from the Superstition Hills, Imperial County, California, earthquakes of 23 and 24 November 1987, *Report No. OSMS 87-06, California Strong Motion Instrumentation Program,* 42 pp.

Hudnut, K. W., L. Seeber, and J. Pacheco (1989). Cross-fault triggering in the November 1987 Superstition Hills earthquake sequence, Southern California, *Geophys. Res. Lett.* **16,** 199–202.

Hwang, L. J., H. Magistrale, and H. Kanamori (1990). Teleseismic source parameters and rupture characteristics of the 24 November 1987, Superstition Hills earthquake, *Bull. Seism. Soc. Am.* **80,** 43–56.

Knopoff, L. (1958). Energy release in earthquake, *Geophys. J.* **1,** 44–52.

Magistrale, H., L. Jones, and H. Kanamori (1989). The Superstition Hills, California, earthquakes of 24 November 1987, *Bull. Seism. Soc. Am.* **79,** 239–251.

Mendoza, C. and S. H. Hartzell (1988a). Inversion for slip distribution using teleseismic *P* waveforms: North Palm Springs, Borah Peak, and Michoacán earthquakes, *Bull. Seism. Soc. Am.* **78,** 1092–1111.

Mendoza, C. and S. H. Hartzell (1988b). Aftershock patterns and main shock faulting, *Bull Seism. Soc. Am.* **78,** 1438–1449.

Olson A. H. and R. J. Apsel (1982). Finite faults and inverse theory with applications to the 1979 Imperial Valley earthquake, *Bull Seism. Soc. Am.* **72,** 1969–2001.

Olson A. H., J. Orcutt, and G. Frazier (1984). The discrete wavenumber/finite element method for synthetic seismograms, *Geophys. J. R. Astr. Soc.* **77,** 421–460.

Porcella, R., E. Etheredge, R. Maley, and J. Switzer (1987). Strong-motion data from the Superstition Hills earthquakes of 0154 and 1315 (GMT), November 24, 1987, *U. S. Geol. Surv. Open-File Rept. 87-672.*

Rymer, M. J. (1989). *Surface rupture in a fault stepover on the Superstition Hills fault, California, U. S. Geol. Surv. Open-File Rept. 89-315,* 309–323.

Sharp, R. V., K. E. Budding, J. Boatwright, M. J. Ader, M. G. Bonilla, M. M. Clark, T. E. Fumal,

K. K. Harms, J. J. Lienkaemper, D. M. Morton, B. J. O'Neill, C. L. Ostergren, D. J. Ponti, M. J. Rymer, J. L. Saxton, and J. D. Sims (1989). Surface faulting along the Superstition Hills fault zone and nearby faults associated with the earthquakes of 24 November 1987, *Bull. Seism. Soc. Am.* **79,** 252–281.

Sipkin, S. A. (1989). Moment-tensor solutions for the 24 November 1987 Superstition Hills, California earthquake, *Bull. Seism. Soc. Am.* **79,** 493–499.

Wald, D. J. and P. G. Somerville (1988). Simulation of accelerograms of the 1987 Superstition Hills earthquake sequence, paper presented at SSA meeting, Honolulu, 24–27 May 1988.

Williams, P. L. and H. W. Magistrale (1989). Slip along the Superstition Hills fault associated with the 24 November 1987 Superstition Hills, California, earthquake, *Bull. Seism. Soc. Am.* **79,** 390–410.

SEISMOLOGICAL LABORATORY
CALIFORNIA INSTITUTE OF TECHNOLOGY
PASADENA, CALIFORNIA 91125
(D.J.W., D.V.H)

UNITED STATES GEOLOGICAL SURVEY
MS 966, BOX 25046
DENVER, COLORADO 80225
(S.H.H)

Manuscript received 26 January, 1990